Catal. Sci. Technol.

ARTICLE

Experimental and DFT Study on Sr doped LaMnO$_3$ Catalyst for NO$_x$ Storage and Reduction

Yue Peng,[a, b] Wenzhe Si,[a] Junhua Li,[*a] John Crittenden[*b] and Jiming Hao[a]

The ideas of rational design of perovskite catalysts for NO$_x$ storage and reduction (NSR) are first from DFT studies on Sr-doped LaMnO$_3$ (001) plane models: Mn-terminated plane (Mn-ter) has a higher activity than La- or Sr-ter planes; the number of A-site defects increases when Sr is doped on; O-vacancy formation energies of both La- and Mn-ter gradually decrease with elevated Sr loading, and the values of La-ter are always larger than Mn-ter at the same Sr loading, indicating that the O-vacancy is facile on Mn-ter with Sr doping. This model yields the highest reactivity for oxidation and the lowest energy barrier for O-vacancy formation. A surface tuning method on La$_{0.5}$Sr$_{0.5}$MnO$_3$ is introduced. With the exception of the promotion of surface area and pore volume, the ratio of Sr/La, number of surface-active oxygen and Mn^{4+} cations most exposed out-layers are also improved with an increased contact time of raw materials with dilute HNO$_3$. However, overtreatment leads to a less stable phase of MnO$_2$ with high reducibility but a significantly restrained NO$_x$ adsorption. NSR performances under lean-burn/fuel-rich cycles are detected, and the results correspond well with NO adsorption or oxidation behaviors and DFT calculations.

Introduction

Nitrogen oxides (NO$_x$) are among the major air pollutants emitted from power plants and diesel vehicles. Selective catalytic reduction of NO$_x$ with NH$_3$ is demonstrated to be effective for power plant exhaust gas, while the NO$_x$ storage reduction (NSR) technology is a promising method to eliminate NO$_x$ from diesel vehicles [1-3]. In a common NSR catalyst, Pt/BaO/Al$_2$O$_3$, NO is oxidized to NO$_2$ on Pt and subsequently adsorbed on BaO as nitrate species in the lean-burn period [4, 5]. During the short fuel-rich period, hydrocarbons are supplied to reduce NO$_x$ to N$_2$. Recently, Sr-doped perovskite oxides (ABO$_3$) were discovered to be efficient platinum substitutes in diesel oxidation and NSR reactions [6]. A-sites of perovskite, such as La or Sr, are good sites for NO$_x$ adsorption and B-sites (Mn or Co) are high active for NO oxidation [7, 8]. The oxidation activity depends on the reducibility, oxygen mobility within the lattice, and the surface defects [9-11].

There are two problems that need to be resolved for the applications of these catalysts. Catalysts synthesized by traditional method have low surface areas and large particle size, thereby preventing adequate contact between gaseous NO$_x$ and active sites. One of the solutions is to use polymeric materials as soft templates for the preparation of porous perovskite [12-14]. Though this method increases the surface area up to 60 m^2/g, the templates are too expensive for large scale production in industry. Developing economical methods for perovskite synthesis remains a challenge. Another problem is determining how to modify the catalyst surface to expose most of the active sites for efficient NO$_x$ adsorption and reduction. The facile strategy is doping alkali or rare-earth metals to A-sites and transitional or precious metals to B-sites, which improves the reducibility of B-sites and provides surface-active oxygen [15, 16]. However, the optimized redox sites cannot be easily observed due to nonstoichiometric nature of perovskite.

This property limits the control over particle size and distribution, as well as the surface anchorage [11]. Therefore, it is necessary to design reasonable models to predict these critical properties of perovskite for a given reaction.

Density functional theory (DFT) is a powerful tool to elucidate the electronic structures of catalytic surfaces and their reactivity [17, 18]. Researchers are also interested in the structure of perovskite models. The (001) plane of LaMnO$_3$ plays an important role in oxygen-related processes. MnO$_2$ [001] is found to be the most stable termination for a solid oxide fuel cell, and the interaction of O with a surface O-vacancy is the rate-determining step for an oxidation reaction [19-23]. Recently, it has been reported that Sr could increase the oxidation ability and diminish the inhibition of NO$_2$ for La$_{1-x}$SrCoO$_3$. In addition, the formation of vacancy sites is more facile on CoO$_2$-terminated surfaces [19]. However, a systematic DFT study on LaMnO$_3$ perovskite, especially the relationship between electronic structures and reducibility, remains incomplete.

In this work, we employed DFT calculations to study basic properties for a NSR reaction on Sr-doped LaMnO$_3$ (001) planes and subsequently introduced a surface tuning method to modulate the La$_{0.5}$Sr$_{0.5}$MnO$_3$ catalysts. After characterizations by H$_2$-TPR and XPS spectra, the actual NSR performance under alternating lean-burn/fuel-rich cycles was also studied.

Experimental

Models selection and DFT details

For theoretical calculations, we employed the *ab initio* DFT plane wave based Materials Studio 5.5. The generalized gradient approximation plus Hubbard model (GGA+U), according to Perdew, Burke, and Ernzerhof was employed [24-26],

where the value of U was set to be 5.0 for Mn [27]. The typical plane wave cut-off energy was E_{cut}=450 eV and the spin polarizations were also applied. The Monkhorst-Pack division scheme was selected to generate a set of k-points within the Brillouin zone.

Models were cut from the (001) plane of $LaMnO_3$ bulk with a lattice constant, a=3.88 Å and a space group, *Pm3m*. We selected the seven-layer slab for geometry optimization, where the periodically repeated slabs were separated by a vacuum gap of 15 Å, as shown in the supporting information. The slabs were terminated by different planes: La-O and Mn-O were denoted as La-ter and Mn-ter, respectively. A Sr-doped plane was constructed by replacing the outmost layer and sub-outmost layer La for Sr on La-ter and Mn-ter models. The models were denoted as Sr-ter and Sr-Mn-ter (**Fig. 1**). To study the electronic structures of A-sites defects, we deleted one surface La and Sr atom on La-ter and Sr-ter models. In addition, 1 to 4 surface La cations were substituted for Sr to study the O-vacancies and their formation energy (E_v). The E_v is calculated as:

$$E_v = E(LSM_v) + \frac{1}{2}E(O_2) - E(LSM) \qquad (1),$$

$E(LSM_v)$ was the energy of the reduced slab by removing a surface oxygen atom, $E(O_2)$ was the energy of oxygen, and $E(LSM)$ was the energy of the slab. It is important to note that the small value of E_v indicates the ease of forming O-vacancy.
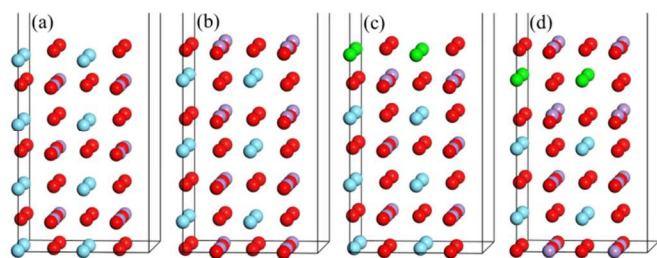

Fig. 1. The optimized structures of (a) La-ter, (b) Mn-ter and corresponding Sr doped (c) Sr-ter and (d) Sr-Mn-ter perovskite (001) planes. Cyan balls are La, purple balls are Mn , green balls are Sr and red ball are oxygen.

Catalyst preparation

Perovskite was synthesized by a hydrothermal method. $La(NO_3)_3$, $Sr(NO_3)_2$, $KMnO_4$, and $MnCl_2$ were mixed with a 20 g KOH solution with stirring. The solution was transferred to a stainless steel lined Teflon vessel for hydrothermal treatment at 260 °C for 24 h, and then the precipitation was washed and dried at 60 °C. The precipitate was crushed and sieved with meshes >60 times, followed by the use of a catalyst surface modification method to dissolve the sample to 3M HNO_3 for different lengths of time. The samples were first dried and then calcined at 400 °C for 2 h. The raw catalyst was denoted as LSM1, and the samples treated with dilute HNO_3 for 10 min, 1 h, and 10 h were denoted as LSM2, LSM3, and LSM4, respectively.

Catalyst characterization

BET surface area of the samples was carried out with a Micromeritics ASAP 2020 apparatus. The crystal structure was determined using XRD measurements (Rigaku, D/max-2200/PC) between 20° and 80° at a step rate of 10°/min, operating at 40 kV and 30 mA, using CuKα radiation. A SEM image was graphed with a Helios NanoLab 600i Dual Beam System, FEI Company. XPS was performed with an ESCALab220i-XL electron spectrometer from VG Scientific using 300 W Al Kα radiations. The binding energy is referenced to the C1s line at 284.8 eV. The bulk element atomic compositions are characterized by ICP-AES with an IRIS Intrepid II XSP apparatus (Thermo Fisher Scientific Inc.). H_2-TPR was performed on a ChemiSorb 2720 TPx chemisorption analyzer under 10 % H_2/Ar gas flow (50 mL/min), at a rate of 10 °C/min, up to 1000 °C. The H_2 consumption of each catalyst preparation was calculated by comparison with that of a standard CuO sample.

NSR tests

NO oxidation measurements were performed in a fixed-bed quartz reactor using 100 mg of the catalyst. The feed gas mixture contained 500 ppm NO and 3 % O_2 and the balance was N_2. NO-TPD was performed in a fixed-bed quartz reactor. Samples were purged under 1000 ppm NO at room temperature, after being pretreated in N_2 at 350 °C for 1 h. After isothermal removal physical adsorbed NO, the temperature increased to 600 °C at a rate of 10 °C·min^{-1}. The lean/rich cycles were evaluated at 250 °C in the alternative lean-burn (500 ppm NO, 5 % O_2) and fuel-rich (500 ppm NO, 1000 ppm C_3H_6) atmosphere. The total flow rate was 200 mL/min. The concentrations of the gases (NO, NO_2, and C_3H_6) were continually monitored by an FTIR spectrometer (MultiGas TM 2030 FTIR). To better evaluate the catalytic activity, kinetic parameters were calculated according to the following equation, applied with the NO conversion:

$$k = -\frac{V}{W} \times ln(1-x) \qquad (2),$$

where k is the reaction rate constant (mL/g·s), V is the total gas flow rate (mL/s), W is the mass of catalyst in the reactor, and x is the NO conversion. The apparent activation energy was calculated using the Arrhenius equation, which is given by:

$$k = k_0 e^{-E_a/RT} \qquad (3),$$

E_a is the energy barrier, and it can be calculated from the slope of the ln(k) versus 1/T curve as the inset.

Results and discussion

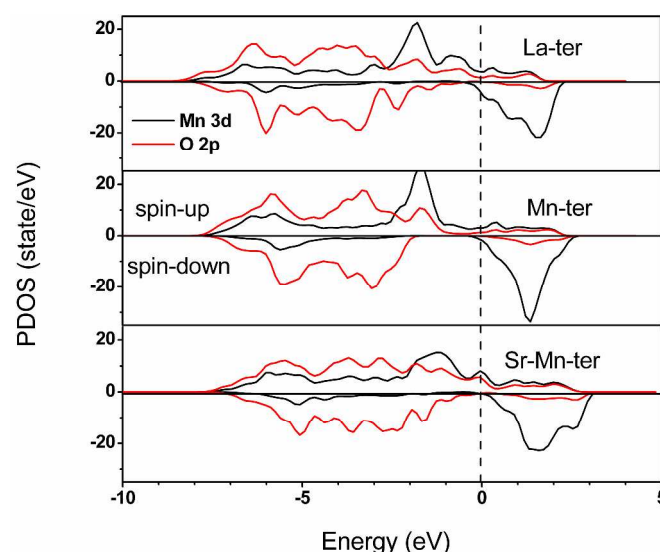**Influence of exposed surfaces, dopants, and A-site defects**

Fig. 2. Projected density of state (PDOS) of (a) Mn 3d and O 2p orbitals over La-ter, Mn-ter and Sr-Mn-ter models.

As can be observed in **Fig. 2**, the PDOS of Mn 3d contained a valence band (VB) at -7.5 eV<E<0 and a conduction band (CB) up to 3.0 eV without a strict band gap. PDOS for spin-up and spin-down states were considerably different for Mn 3d on both sides of the Fermi energy (E=0), while O 2p showed a lower state at these regions. One can conclude from the contribution of Mn and O states to PDOS that the ionic bond, rather than covalent component of the Mn-O bond, grew from the lowest surface band to the top of VB, even though the Mn-O bond did not expose the outmost (La-ter). The large polarization of Mn 3d states from the small hopping integrals between ions' and neighboring site electrons led to the strong ionic interaction through the bridged oxygen between Mn [28]. Compared to the top of VB of Mn 3d between La-ter and Mn-ter, a slight movement to higher energy was observed from -1.74 eV to -1.65 eV, indicating that the Mn 3d states of Mn-ter exhibit higher binding to surface than those of La-ter.
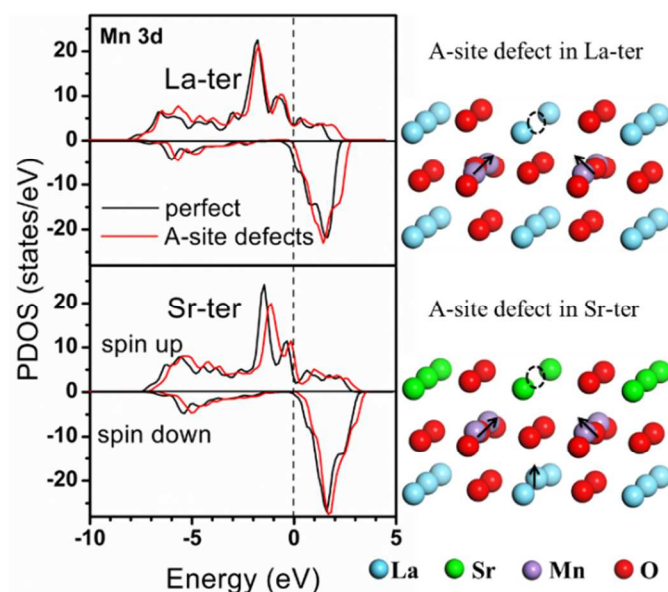

Fig. 3. PDOS Mn 3d orbitals over La-ter, Sr-ter and A-site defect models and the front view of the defect models.

A new impurity level of Sr-Mn-ter occurred across the Fermi energy, and the blueshift of VB became more apparent than that of Mn-ter. The results imply that Mn in the perovskite lattice might has a higher reactivity when it is exposed on the outmost layer and could be further improved by Sr. That is, to enhance the activity of perovskite during the oxidation process, more Mn-O need to be exposed, and the dopants such as Sr are necessary to modify the proportion of the A-site.

Fig. 3 demonstrates PDOS of La-ter and Sr-ter planes and their corresponding A-site defects (Ad) models, where a surface La or Sr cations was removed (dashed circle on the right side of the figure). Mn 3d states of La-ter were nearly unchanged by eliminating La. Only the end of CB shifted 0.5 eV to higher energy. Mn cations on the sub-outmost layer of La-ter with Ad moved toward the defect site to some extent (indicated by the arrow). In comparison with Mn 3d states of Sr-ter, the top of VB and impurity level of the Ad model shifted to the Fermi energy, and the bottom of CB only presented slight changes. The Ad of Sr-ter also showed differences from the Ad of La-ter model. In addition to the movement of Mn cations towards the defect site, La on the third layer also moved up to the defect site. The results indicate that Mn on the sub-outmost layer can be

activated by the formation of A-site defects and can be further improved by dopant Sr.

O-vacancy formation energy

To obtain directly the relationship between oxidation activity and the influence factors discussed above, we calculated the O-vacancy formation energy (E_v) on both La-ter and Mn-ter models with different Sr coverage (**Fig. 4**). E_v values of La-ter were greater than those of Mn-ter for all Sr doping models, suggesting that O-vacancy preferred to form on Mn-ter surface, rather than La-ter surface, i.e., Mn-ter surfaces have higher oxygen storage/release capacity, thereby increasing the oxidation activity during the reaction process. The results are in agreement with the discussion of electronic structures in **Fig. 2**. With increased Sr loading, E_v values of both La-ter and Mn-ter decreased. The lowest value was less than 2.0 eV for Sr-Mn-ter (the sub-outmost layers were "totally" covered by Sr). It is important to note that we could not prepare $La_xSr_{1-x}MnO_3$ materials with all of the Sr cations exposed at the outmost layer because high levels of $SrCO_3$ blocks the perovskite surface when excess $Sr(NO_3)_2$ precursors are introduced during the preparation [29, 30]. Therefore, these results above are only applicable for the DFT modeling. However, most researchers have also tried to synthesize $La_xSr_{1-x}MnO_3$ with high Sr loading, and they found that the value of Sr between 0.3 and 0.5 seemed better for the oxidation reaction [7, 31, 32]. Overall, the effect of Sr is to promote the oxidation activity and O-vacancy formation of $LaMnO_3$ (001) planes. The absolute value of E_v of La-ter and Mn-ter enlarged with increased Sr loading, revealing that the improvement of Sr is greater on Mn-ter than on La-ter. Consequently, the surface exposed Mn-O bondage has higher oxidation activity than that of exposed La-O or Sr-O bonds.
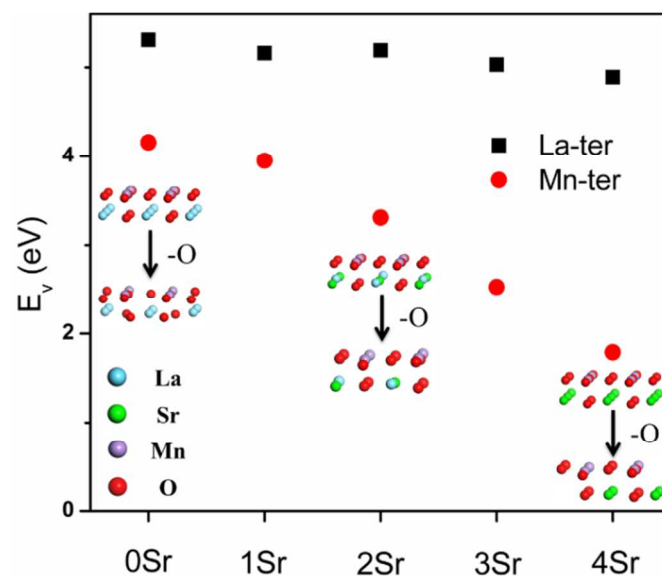

Fig. 4. O-vacancy formation energy (E_v) for La-ter and Mn-ter models with increasing Sr doping loadings.

In summary, in addition to controlling catalyst surface areas or pore volumes, Sr improves the number of adsorption site, modifies the surfaces with A-site defects, and enhances the reactivity of Mn cations. Moreover, the surface with terminated Mn has a higher activity than those with terminated La or Sr, and the surface oxygen has higher mobility (low E_v) with more Sr doped on the terminated Mn surface. However, one must

note that in the NSR reaction, enough amounts of alkali metals are necessary for NO adsorption directly from the gas phase or NO_2 adsorption from oxidation sites. The following works are based on the results that improved the properties of the NSR reaction [33].
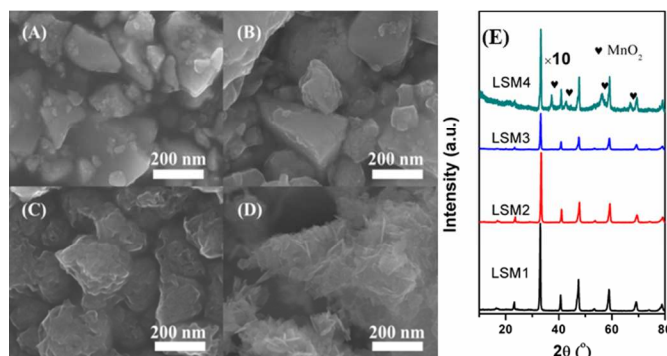
Physic-chemical properties of perovskite

Fig. 5. SEM images and XRD patterns of the catalysts.

Fig. 5 presents XRD patterns and SEM images over LSM1 to LSM4 catalysts, respectively. SEM images showed that some layer clusters grew up from bulk materials (LSM2) and became considerable on LSM3, and large amount of clusters were observed on LSM4. Combined with XRD patterns, these clusters might be MnO_2 oxides. Main peaks of LSM1 to LSM3 are attributed to the standard perovskite phase (a= 3.88 Å with space group *Pm3m*), which exhibits a good accordance with the bulk model used in DFT. LSM4 displayed low crystallization compared to the other three samples, and MnO_2 diffraction peaks appear. Except for MnO_2, both La_2O_3 and SrO are soluble in dilute HNO_3. With increased contact time, more A-site cations run away from perovskite structures and only MnO_2 is left on the surface of materials.
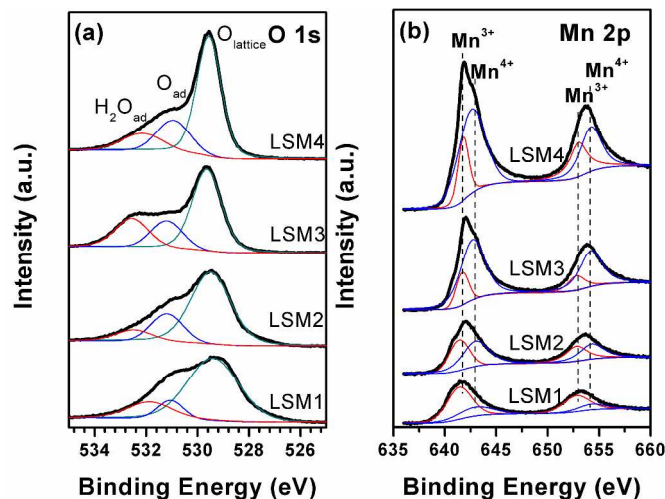

Fig. 6. (a) O 2p and (b) Mn 3d spectra of XPS of the catalysts.

Table 1 lists SA, Pv and element ratios of Sr/La for both bulk and surface, which were all improved with increased contact time of raw materials with dilute HNO_3. The surface areas were from 0.36 m^2/g for LSM1 to 67.15 m^2/g for LSM4. Pore volumes of the catalysts presented the same trend. We also prepared another portion of samples for a 72 h treatment as well, with a surface area of 178.95 m^2/g, and a crystal phase which is

mainly β-MnO_2 after calcined at 400 °C, indicating this modulate method is effective on enlarging materials' surface area and pores.

Table 1. Surface area (SA), pore volume (Pv), element atomic ratio of Sr and La, proportion of surface adsorbed oxygen, Mn^{4+} determined by XPS over the four perovskite materials.

sample	SA (m^2/g)	Pv (cm^3/g)	Sr/La[a]	Sr/La[b]	O_{ad}/O_{latt} (%)[b]	Mn^{4+}/Mn^{3+} (%)[b]
LSM1	0.36	0.02	0.90	0.80	13.7	42.0
LSM2	5.90	0.03	0.92	0.94	27.9	62.8
LSM3	22.22	0.09	0.93	0.99	32.1	63.7
LSM4	67.15	0.20	1.01	1.10	33.9	65.8

[a] calculated from ICP results of catalyst powder
[b] calculated from XPS spectra

The ratios of surface-active oxygen and Mn^{4+} cations were calculated from XPS spectra (**Fig. 6**) and summarized in **Table 1**. The O 1s peaks can be fitted into two peaks, referred to as the lattice oxygen at 529.3–530.3 eV (O_{latt}) and chemisorbed surface oxygen at 530.9–531.9 eV (O_{ad}). O_{ad} is highly active in oxidation reactions due to its higher mobility than the lattice oxygen O_{latt} [33]. The spectra of Mn 2p can be also fitted into two peaks, attributing to Mn^{3+} (641.1 and 652.8 eV) and Mn^{4+} (643.0 and 654.3 eV) respectively [29]. They were both enhanced by elevating the contact time: LSM1 only had 13.7 % of O_{ad}/O_{latt} and 42.0 % of Mn^{4+}/Mn^{3+}, while LSM4 yielded 33.9 % of O_{ad}/O_{latt} and 65.8 % Mn^{4+}/Mn^{3+}. Combined with the DFT results, this tuning method increases both the number of surface-active oxygen and the concentration of Mn^{4+} cations, leading to more O-vacancy formation [34].

Fig. 7 illustrates the H_2-TPR profiles of the catalysts. Two broad bands centered at 505 °C and 755 °C of LSM1 can be attributed to the reduction of Mn^{4+} to Mn^{3+} for charge compensation from Sr incorporation, and the reduction of Mn^{3+} to Mn^{2+}, respectively [34-36]. With an increased contact time, the peak at 505 °C of LSM1 shifted to a lower temperature, at 397 °C of LSM4. Another new peak centered at 293 °C appeared for LSM3 and considerably grew for LSM4. Combined with the structural characterization, this reduction peak was mainly from the contribution of MnO_2 (Mn^{4+} to Mn^{3+}). Previous work on a comparative study on α-Mn_2O_3 and β-MnO_2 obtained similar TPR peaks at approximately 300 °C on pure β-MnO_2 material [37]. By calculating the ratio of H_2 consumption, this peak was attributed to the reduction of MnO_2 to Mn_3O_4, i.e., partial reduction of β-MnO_2. Therefore, this peak can be specifically attributed to the reduction of Mn^{4+} to Mn^{3+} on MnO_2 surfaces, and the peaks in the range of 397 °C to 505 °C for samples were due to the reduction of Mn^{4+} on the perovskite surface. The H_2 consumption peaks for the catalysts are also listed in the **Table 2** and were enhanced with increased contact time. That is, the method improved both the quantity (peak area) and reducibility (peak position) of Mn^{4+} cations on the perovskite.

Table 2. H_2 consumption calculated by H_2-TPR profiles.

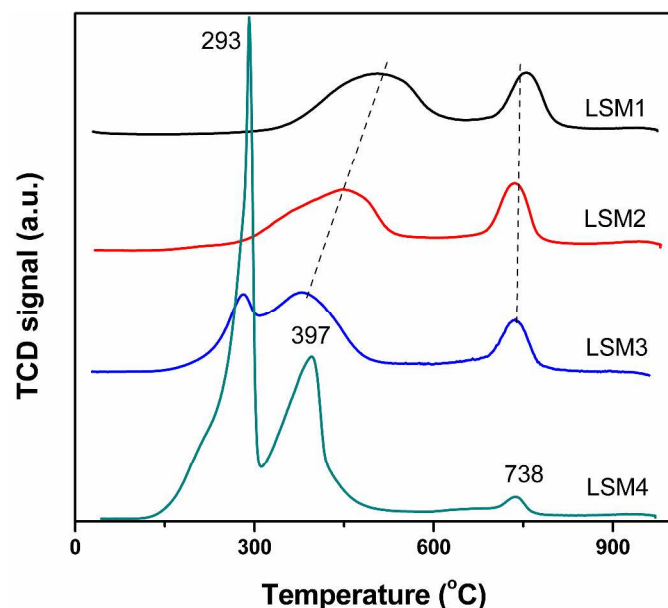| sample	H_2 consumption (a.u.)		
	<300 °C	<600 °C	<800 °C
LSM1	0	10.0	4.5
LSM2	0	11.1	5.7
LSM3	5.0	11.4	4.0
LSM4	20.6	13.8	1.0

Fig. 7. H$_2$-TPR profiles of perovskite materials in the temperature range of 30-1000 °C.

NSR performance

Fig. 8(a) displays the Arrhenius plots of NO oxidation over the samples. The apparent energy barrier for LSM1 was relatively high (72.7 kJ/mol), however the energy barriers of other samples were within 44-50 kJ/mol and only a slight decrease appeared between LSM3 and LSM4. The results demonstrated that with increased Mn^{4+} cations and surface-active oxygen, NO oxidation activity is significantly improved. Moreover, apart from the oxidation ability, NO$_x$ adsorption is another important property for NSR technology.
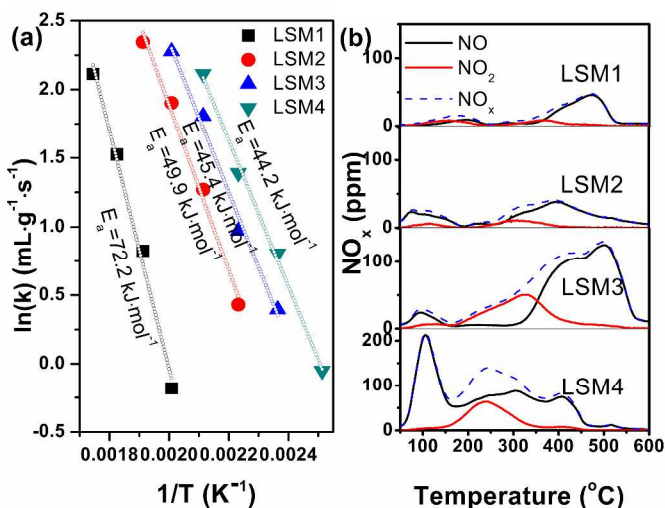

Fig. 8. (a) Arrhenius plot of NO oxidation and (b) NO-TPD profiles of perovskite materials.

Fig. 8(b) presents the NO-TPD profiles of the four samples in the temperature of 50-600 °C and the total NO desorption normalized by surface area are listed in **Table 3**. The total NO$_x$ desorption significantly decreased with an increased contact time, suggesting the adsorption sites for NO$_x$ are not improved by surface tuning. Considering the decrease of La and Sr

element proportion, it can be concluded that the major adsorption sites for NO$_x$ are La or Sr cations, rather than Mn cations or MnO$_2$. Moreover, the Sr loading from ICP and XPS exhibited the same value as LSM3 and LSM4. It might be resulted from that only parts of the Sr are successfully doped in the lattice of perovskite and the remnant are formed SrCO$_3$ during preparation process. With increased the contact time, most SrCO$_3$ is dissolved in HNO$_3$ and the remaining Sr cations are enriched on the surface of materials. Two NO peaks and a NO$_2$ peak can be observed on the NO-TPD profiles for the catalysts. The low temperature NO peak (below 300 °C) can be attributed to the weak adsorbed NO or nitrite species, the high temperature NO peak can be attributed to the nitrite or nitrate species with strong bondage, and NO$_2$ desorption peak can be attributed to nitrate species [38, 39]. In comparison with the peaks of LSM4 and LSM3, the amount of low temperature NO peak increased significantly. However, the quantity of high temperature NO peak decreased, even it was normalized by the surface area. Based on the crystal structures of the two samples, low temperature peak is tentatively assigned to NO adsorption on MnO$_2$, on which easily desorbed at 200 °C and it seems ineffective for NSR process (stable adsorption above 250 °C). The concentrations of NO$_2$ are enhanced on LSM4, which shows a good agreement with the NO oxidation.

Table 3. Elements atomic compositions of Sr, La and Mn and total NO$_x$ desorption calculated by NO-TPD over the four perovskite materials.

Sample	Sr loading (%)		La loading (%)		Mn loading (%)		NO$_x$ (mmol/m^2)[a]
	ICP	XPS	ICP	XPS	ICP	XPS	
LSM1	13.0	27.1	14.4	33.9	23.0	39.0	2.19
LSM2	12.9	25.8	14.0	27.4	23.4	46.8	0.19
LSM3	10.6	10.0	11.4	10.1	24.5	67.5	0.14
LSM4	4.0	4.1	4.0	3.7	29.2	83.2	0.06

[a] calculated from NO-TPD normalized by SA

The NO adsorption/desorption behaviors of the samples were determined in the periodically alternative lean-burn/fuel-rich atmosphere as shown in **Fig. 9**. After the samples reach steady states, LSM1 only provides limited NO capture: Seventy percent of NO escapes out of the reactor directly, and NO$_2$ reaches equilibrium within 1 min. For LSM2 and LSM3, the escaped NO concentrations are nearly 100 ppm. The equilibrium time of NO$_2$ in a lean-burn period is reduced; approximately 2 min for LSM2 and 1.5 min for LSM3. The results indicate that increased contacting time on catalysts could improve the NO storage process. Only a slight quantity of NO is obtained for LSM4 and NO$_2$ does not achieve a steady concentration within 3 min, implying that LSM4 catalyst exhibits the best NO oxidation activity among the samples. The improvement of this NSR performance is originated from the synergistic effect of positive factors: increase of surface area, surface-active oxygen and Mn^{4+} cations, as well as negative factors, such as decrease of adsorption sites. Under the fuel-rich condition, the trapped NO$_x$ is released and reduced by C$_3$H$_6$ and no N$_2$O is detected during the entire period. The NO$_x$ maximums of samples were improved with increased contacting time, suggesting the NO oxidation ability was enhanced.

The outlet C$_3$H$_6$ peaks significantly decreased: nearly 800 ppm for LSM1 and 150 ppm for LSM4, indicating that more C$_3$H$_6$ can react with the trapped NO$_x$ to fulfill the NSR process.

The NO concentrations of samples increased under fuel-rich period, which shows the same trending as NO-TPD results. Moreover, the peak of NO widened for LSM4 compared with LSM2 and LSM3, indicating that perovskite with excess MnO_2 decreases the NSR performance. This can be accounted for the lacking of effective adsorption sites such as alkali metals on MnO_2, the adsorption process of NO is weak and easily desorbed from the surface of MnO_2 under NSR working temperature (250-300 °C). NO-TPD profiles of LSM4 also show the similar results.
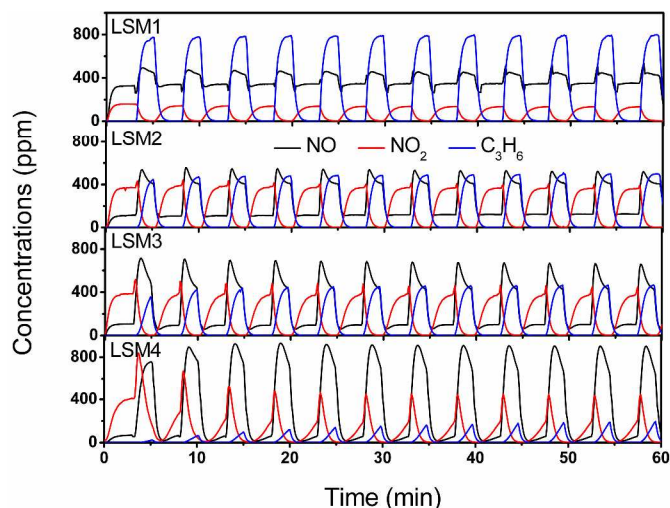

Fig. 9. Lean/rich cycles of the perovskite materials operated at 300 °C. Lean-burn period: 3 min, gas composition: 500 ppm NO/5 % O_2; fuel-rich period: 2 min, gas composition: 500 ppm NO/1000 ppm C_3H_6.

Conclusions

Combined DFT calculations with experiments results, three aspects of $La_xSr_{1-x}MnO_3$ catalyst are modulated and evaluated for the NSR technology:

(1). Surface area and pore volume of catalysts are increased by the modification process because of the corrosion effect of dilute HNO_3 to La_2O_3 and SrO rather than MnO_2, which provides more effective surfaces for the NO_x adsorption or oxidation;

(2). La or Sr cations in the outmost layer of perovskite are removed by the modification process, promoting the number of O-vacancy and the reactivity of Mn^{4+} cations in the perovskite lattice. From the calculated models, Mn-terminated surface with Sr doped on A-site of $LaMnO_3$ (001) plane yields the highest activity for oxidation and the lowest energy barrier for O-vacancy formation, which exhibits good accordance with apparent energies barriers of NO oxidation;

(3). The crystallized MnO_2 oxides might form on the outmost layer of perovskite if the contacting time with HNO_3 becomes too long. Though the reducibility of material is further enhanced, NO adsorption sites dramatically decrease even normalized by the surface area. The adsorbed NO_x are unstable and easily desorb from catalysts surface, leading to the blockage of NO adsorption in NSR process.

Therefore, we tentatively propose the goal of rationally designing perovskite catalysts for NSR technology: to improve surface area or pore volume, exposing more transitional metals in the outmost layer of catalysts, which could provide adequate adsorption sites and increase the doping amount to the catalyst. This improvement could result in $SrCO_3$ crystallization on the surface to cover the oxidation sites.

Notes and references

[a] State Key Joint Laboratory of Environment Simulation and Pollution Control, School of Environment, Tsinghua University, Beijing, 100084, China.
[b] School of Civil and Environmental Engineering, Georgia Institute of Technology, Atlanta, Georgia, 30332-0595, United States
[*] Corresponding authors
Tel. & Fax: +86 10 62771093; +1 404-894-5676.
E-mail addresses: lijunhua@tsinghua.edu.cn;
                  john.crittenden@ce.gatech.edu.

1. F. Prinetto, G. Ghiotti, I. Nova, L. Lietti, E. Tronconi, P. Forzatti, *J. Phys. Chem. B*, 2001, 105, 12732-12745.
2. N. Phuc, X. Courtois, F. Can, S. Berland, S. Royer, P. Marecot, D. Duprez, *Catal. Today*, 2011, 176, 424-428.
3. F. Frola, M. Manzoli, F. Prinetto, G. Ghiotti, L. Castoldi, L. Lietti, *J. Phys. Chem. C*, 2008, 112, 12869-12878.
4. C. DiGiulio, V. Komvokis, M. Amiridis, *Catal. Today*, 2012, 184, 8-19.
5. N. Phuc, X. Courtois, F. Can, S. Royer, P. Marecot, D. Duprez, *Appl. Catal. B*, 2011, 102, 353-361.
6. C. Kim, G. Qi, K. Dahlberg, W Li, *Science*, 2010, 327, 1624-1627.
7. X. Li, Y. Dong, H. Xian, W. Hernandez, M. Meng, H. Zou, A. Ma, T. Zhang, Z. Jiang, N. Tsubaki, P. Vernoux, *Energy Environ. Sci.*, 2011, 4, 3351-3354.
8. L. Guo, H. Xian, Q. Li, D. Chen, Y. Tan, J. Zhang, L. Zheng, X. Li, *J. Hazard. Mater.*, 2013, 260, 543-551.
9. M. Pena, J. Fierro, *Chem. Rev.*, 2001, 101, 1981-2018.
10. J. Zhu, H. Li, L. Zhong, P. Xiao, X. Xu, X. Yang, Z. Zhao, J. Li, *ACS Catal.*, 2014, 4, 2917-2940.
11. D. Neagu, G. Tsekouras, D. Miller, H. Ménard, J Irvine, *J. Nat. Chem.*, 2013, 5, 916-923.
12. J. Xu, J. Liu, Z. Zhao, J. Zheng, G. Zhang, A. Duan, G. Jiang, *Catal. Today*, 2010, 153, 136-142.
13. H. Arandiyan, H. Dai, J. Deng, Y. Wang, H. Sun, S. Xie, B. Bai, Y. Liu, K. Ji, L. Li, *J. Phys. Chem. C*, 2014, 118, 14913-14928.
14. Y. Liu, H. Dai, Y. Du, J. Deng, L. Zhang, Z. Zhao, *Appl. Catal. B*, 2012, 119-120, 20-31.
15. T. Ishihara, H. Matsuda, Y. Takita, *JACS*, 1994, 116, 3801-3803.
16. E. Edri, S. Kirmayer, M. Kulbak, G. Hodes, D. Cahen, *J. Phys. Chem. Lett.*, 2014, 5, 429-433.

17. P. Maitarad, D. Zhang, R. Gao, L. Shi, H. Li, L. Huang, T. Rungrotmongkol, J. Zhang, *J. Phys. Chem. C*, 2013, 117, 9999-10006.
18. P. Maitarad, J. Han, D. Zhang, L. Shi, S. Namuangruk, T. Rungrotmongkol, *J. Phys. Chem. C*, 2014, 118, 9612-9620.
19. S. Choi, M. Penninger, C. Kim, W. Schneider, L. Thompson, L. *ACS Catal.*, 2013, 3, 2719-2728.
20. E. Kotomin, R. Evarestov, Y. Mastrikov, J. Maier, *Phys. Chem. Chem. Phys.*, 2005, 7, 2346-2350.
21. E. Kotomin, Y. Mastrikov, E. Heifets, J. Maier, *Phys. Chem. Chem. Phys.*, 2008, 10, 4644-4649.
22. Y. Mastrikov, E. Heifets, E. Kotomin, J. Maier, *Surf. Sci.*, 2009, 603, 326-335.
23. M. Kuklja, E. Kotomin, R. Merkle, Y. Mastrikov, J. Maier, *Phys. Chem. Chem. Phys.*, 2013, 15, 5443-5471.
24. A. Becke, *Phys. Rev. A*, 1988, 38, 3098-3100.
25. B. Delley, *J. Chem. Phys.*, 1990, 92, 508-517.
26. J. Perdew, K. Burke, M. Ernzerhof, *Phys. Rev. Lett.*, 1996, 77, 3865-3868.
27. C. Sun, Y. Wang, J. Zou, S. Smith, *Phys. Chem. Chem. Phys.*, 2011, 13, 11325-11328.
28. V. Avdeev, V. Tapilin, *J. Phys. Chem. C*, 2010, 114, 3609-3613.
29. F. Teng, W. Han, S. Liang, B. Gaugeu, R. Zong, Y. Zhu, *J. Catal.*, 2007, 250, 1-11.
30. S. Liang, F. Teng, G. Bulgan, Y. Zhu, *J. Phys. Chem. C*, 2007, 111, 16742-16749.
31. M. Zhi, G. Zhou, Z. Hong, J. Wang, R. Gemmen, K. Gerdes, A. Manivannan, D. Ma, N. Wu, *Energy Environ. Sci.*, 2011, 4, 139-144.
32. M. Jong, I. Bergenti, W. Osikowicz, R. Friedlein, V. Dediu, C. Taliani, W. Salaneck, W. *Phys. Rev. B*, 2006, 73, 052403.
33. K. Huang, X. Chu, L. Yuan, W. Feng, X. Wu, X. Wang, S. Feng, *Chem. Comm.*, 2014, 50, 9200-9203.
34. K. Huang, X. Chu, W. Feng, C. Zhou, W. Si, X. Wu, L. Yuan, S. Feng, *Chem. Eng. J.*, 2014, 244, 27-32.
35. E. Crumlin, E. Mutoro, Z. Liu, M. Grass, M. Biegalski, Y. Lee, D. Morgan, H. Christen, H. Bluhm, Y. Shao-Horn, *Energy Environ. Sci.*, 2012, 5, 6081-6088.
36. J. Fierro, J. Tascón, L. Tejuca, *J. Catal.*, 1985, 93, 83-91.
37. X. Tang, J. Li, L. Sun, J. Hao, *Appl. Catal. B*, 2010, 99, 156-162.
38. Y. Peng, J. Li, X. Huang, X. Li, W. Su, X. Sun, D. Wang, J. Hao, *Environ. Sci. Technol.*, 2014, 48, 4515-4520.
39. Y. Peng, C. Liu, X. Zhang, J. Li, *Appl. Catal. B*, 2013, 140-141, 276-282.

Catalysis Science & Technology Accepted Manuscript

Graphical Abstract

By DFT and experiments study on $La_xSr_{1-x}MnO_3$ perovskite, Mn-terminated surface with Sr doped displays good performance on NSR technology.